A Theoretical Analysis of Coherent Cross-Peaks in Polarization Selective 2DIR for Detection of Cross-α Fibrils

Dean N. Edun,[1,a)] Olivia M. Cracchiolo,[1,a)] and Arnaldo L. Serrano [1,b)]

[1] *Department of Chemistry and Biochemistry, University of Notre Dame, Notre Dame, Indiana 46556, United States*

The coupled amide-I vibrational modes in peptide systems such as fibrillar aggregates can often provide a wealth of structural information, though the associated spectra can be difficult to interpret. Using exciton scattering calculations, we characterized the polarization selective 2DIR peak patterns for cross-α peptide fibrils, a challenging system given the similarity between the monomeric and fibrillar structures, and interpret the results in light of recently collected 2D data on the cross-α peptide PSMα3. We find that stacking of α-helices into fibrils couples the bright modes across helical subunits, generating three new Bloch-like extended excitonic states that we designate $A_\perp$, $E_\parallel$, and $E_\perp$. Coherent superpositions of these states in broad-band 2DIR simulations lead to characteristic signals that are sensitive to fibril length, and match the experimental 2DIR spectra.

I. INTRODUCTION

Infrared (IR) spectroscopy is a useful tool protein secondary structure determination due to its ability to probe backbone amide modes without any added labels.[1–3] These modes have been thoroughly studied and are well understood for the most common secondary structures.[4] For example, a mixture of theory and experimental linear vibrational spectroscopy has been used in the past for identifying characteristic features of amyloid fibers, which result from the arrangement of proteins into highly ordered structures.[5–8] However, little is still known about the IR properties of a recently discovered amyloid structure, which is the subject if this study. Phenol Soluble Modulin α3 (PSMα3), a peptide secreted by *Staphylococcus aureus*, forms amyloid-like structures that appear to play an important role in the structural integrity of bacterial biofilms. PSMα3 adopts a native α-helical structure[9,10] in its monomeric form (Figure 1a) which it maintains upon fibril formation, making it the first known example of a peptide fibril possessing α-helical secondary structure. These fibrils, formed from horizontal stacking (Figure 1b) of α-helices about a screw axis of symmetry, have been termed "cross-α fibrils".[10,11] The formation of these cross-α structures raises questions about potential changes in the vibrational spectrum due to increased structural order and potential interhelix coupling. At the same time, the lack of intermolecular hydrogen bonding, a characteristic element of traditional cross-

---

β fibrils, raises concerns about the detectability of this species, as it suggests a lack of well aligned, strongly interacting infrared chromophores. The latter is what lends to amide-I FTIR spectra their sensitivity to protein structure.

In this work, we present detailed FTIR and 2DIR spectroscopic calculations in order to determine the dominant modes responsible for the infrared response, as well as to uncover observables in the spectra that would aid in identifying this newly discovered amyloid structure in other systems. We found that, though the small coupling between helices leads to only minor changes in the FTIR spectra, the relative alignment of the IR active modes of the helices and their interactions proved a signature of cross-α fibril formation in polarization sensitive measurements which is sensitive to fibril length and represents coupling between extended helix *A* and *E* modes. Finally, we interpret our simulation results in light of recently measured experimental 2DIR data of PSMα3.[12]

II. METHODS

We used a floating oscillator model to calculate the vibrational spectra for the peptides.[13] Using, coordinates, for both the monomer and fibril, determined from the crystal structures,[10] we extracted the local transition dipole moments and their corresponding positions in space.[13,14] We calculated the coupling energies between all pairs of local amide groups using transition dipole coupling (TDC), with parameters from Tasumi and Torii.[13,15] We used couplings and local site energies to build the one-quantum Hamiltonian. Diagonal entries of the matrix had a center frequency of 1650 cm^{-1}, with additional random gaussian diagonal disorder possessing a standard deviation 12 cm^{-1}, except where otherwise indicated. We diagonalized the one-quantum Hamiltonian to obtain eigenenergies and eigenvectors.[15] We then calculated exciton transition dipoles by representing them in the local mode basis. FTIR spectra were obtained by scaling each transition by the magnitude squared of its transition dipole moment and summing all modes on a grid and convolving the stick spectrum with a Lorentzian lineshape with a halfwidth of 5 cm^{-1}. A more complete description of the model is included in Appendix A.

Simulations of fibril crystal structures can involve more than 1000 oscillators, causing the vibrational states to be densely packed, making it difficult to choose any particular normal mode as the representative mode for a given frequency region. In order to characterize the main contributions to the spectrum, we used a doorway state representation. To do so, we selected subregions of the spectrum that we wished to characterize. Performing singular value decomposition on a matrix of transition moments of all the eigenmodes within the region provided a unique decomposition of the spectral intensity into 3 orthogonal, bright doorway modes and n-3 dark modes that represent the set of eigenmodes.[16–18] Using this approach, we were able to represent peaks in the spectra as originating from select doorway modes. In the present study, we generally analyzed the properties of the brightest of the three doorway modes. A mathematical description of the doorway state analysis is given in Appendix B.

To simulate the 2DIR spectra, rather than using a more conventional sum over state method, which would require calculation of an intractable number of Feynman diagrams, we followed the exciton scattering approach developed by Mukamel, where the nonlinear response can be modeled by the scattering of two excitons by a local chromophore, under the influence of the local mode anharmonicity, requiring only knowledge of the one-quantum Hamiltonian.[19–21] Appendix C contains details about the exciton scattering method. While only requiring diagonalization of the one-quantum Hamiltonian, the number of scattering events that must be calculated still scales as N^4. The total calculation time required, however, can be significantly shortened by selecting only the pathways which contribute significantly to the spectrum. As shown by Mukamel, exploiting the local nature of the excitation and structural arguments, the actual calculation time can be reduced to $O(\sim N^2)$ or even $O(\sim N)$.[19,22] To reduce the number of scatterings calculated, we rejected all pairs of excitons with an exciton overlap factor (Eq. C17) below 0.55. This number was chosen as it is close to the 0.5 cutoff introduced by Mukamel in his demonstration, while still significantly reducing our computation time.[22] The anharmonicity for all sites was set to -15 cm^{-1}. Because each simulation included a different number of total oscillators, they required a different number of realizations of diagonal disorder to produce adequate averaging. Table I lists the numbers oscillators in each structure and the number of realizations of diagonal disorder each 2DIR spectrum was averaged over.

TABLE I. Number of realizations of diagonal disorder averaged over for each structure.

Size of structure simulated	Number of oscillators	Number of realizations	Size of structure simulated	Number of oscillators	Number of realizations
Monomer	21	20	8-unit cells	336	8
1-unit cell	42	10	10-unit cells	420	5
2-unit cells	84	10	20-unit cells	840	3
3-unit cells	126	8	40-unit cells	1680	2
5-unit cells	210	8			

Polarization difference spectra are obtained by normalizing the signals from each of the polarization conditions and subtracting the XXXX spectrum from the XXYY spectrum.

Doorway mode analysis on 2DIR spectra is performed by first simulating 2DIR spectra without diagonal disorder applied. A stricter overlap cutoff of 0.65 was used in these simulations to reduce computation time to a value similar to those with disorder. During the simulation, a list of all combinations of $e_4 e_3 e_2 e_1$ involved in calculating the signal (Eq. C8 and C9) was stored, where e_n is the exciton resonant with the nth excitation in the experiment. We filtered for combinations of e_1 and e_2, corresponding to specific pathways of interest. By only including pathways where e_1 and e_2 have differing fundamental frequencies, we focused on pathways which involved a coherent cross-peak with an oscillation frequency of $|\omega_{e_1} - \omega_{e_2}|$ during T_2. We then stored a list of the transition dipoles involving excitons e_1 and e_2 where the oscillation frequency falls within a

predetermined spectral window. From this list, we perform doorway analysis for both sets of e_1 and e_2 excitons, as described above for the linear spectra. The brightest doorway mode from each set were interpreted as excitonic modes that couple, leading to coherent cross peaks oscillating at $|\omega_{e_1} - \omega_{e_2}|$. From this, we developed a molecular interpretation of the source of coherent signals in the fibril system.

Simulated waiting time spectra are collected by calculating the 2DIR spectrum for an 8-unit fibril with T_2 values starting from 0 ps incremented by 0.5 to 5 ps. The final set of spectra is averaged over 16 realizations of diagonal disorder. Waiting time coherence oscillation spectra are obtained from Fourier transformation of polarization difference spectra along T_w. Only the real part of the Fourier transform is plotted.

III. RESULTS

A. Simulated spectra of PSMα3 fibers

To understand how the structure of cross-α fibers influence the spectral properties of the protein, we used previously a solved x-ray structure to simulate infrared spectra. Figure 1a and b show the monomeric and fibril form of the PSMα3 helices, respectively.[10] The protein fiber has a space group of P2$_1$ where the proteins within the fiber take on a stacked structure extending along a screw axis. To focus on potential spectral signals associated with the formation of this stacked fiber structure we elected to perform simulations using structures where the coordinates are extended along the screw-axis of the crystal.[23]

Figure 1c shows the simulated FTIR spectra for both the monomeric form of the peptide as well as the fibril form, extended 40 peptide units along the screw-axis. Both spectra were calculated without any diagonal disorder to highlight any changes in the peak shapes. The spectra reveal a small splitting between peaks at around 1650 cm^{-1} and 1635 cm^{-1}. These peak positions correspond to the frequencies of the A and the doubly degenerate E_1 normal modes for α-helices. For an ideal α-helical peptide, these are the only IR active amide-I normal modes.[24] In the A mode, all peptide groups oscillate in phase and the transition moment is parallel with the axis of the α-helix. For short helix lengths, the mode has a slightly blue-shifted frequency compared to the frequency of randomly coiled peptide.[16] This peak, however, redshifts with increasing helix length and tends to overlap the random coil peak on average. In general, α-helix A mode peaks are difficult to distinguish from the amide-I band of randomly coiled peptides using FTIR alone, except in the case of highly hydrated helix backbones.[25] The weaker doubly degenerate E_1 modes are made up of amide-I vibrations along the helix with a periodic phase of $2\pi n/m$ where n is the peptide group index and m is the number of residues per turn. The E_1 mode has been calculated to have a frequency near 1655,[26] but the peak frequencies can also shift depending on helix length and local disorder.[16,27] Because the local amide-modes are oriented mostly along the axis of the helix, the E_1 modes are generally weak. The inability to distinguish important structural information

about a protein using FTIR alone leads us to examine the structure using 2DIR methods which have proven well suited for examining α-helix structures.[28-30] But first, we analyze the FTIR simulation results using doorway state analysis.
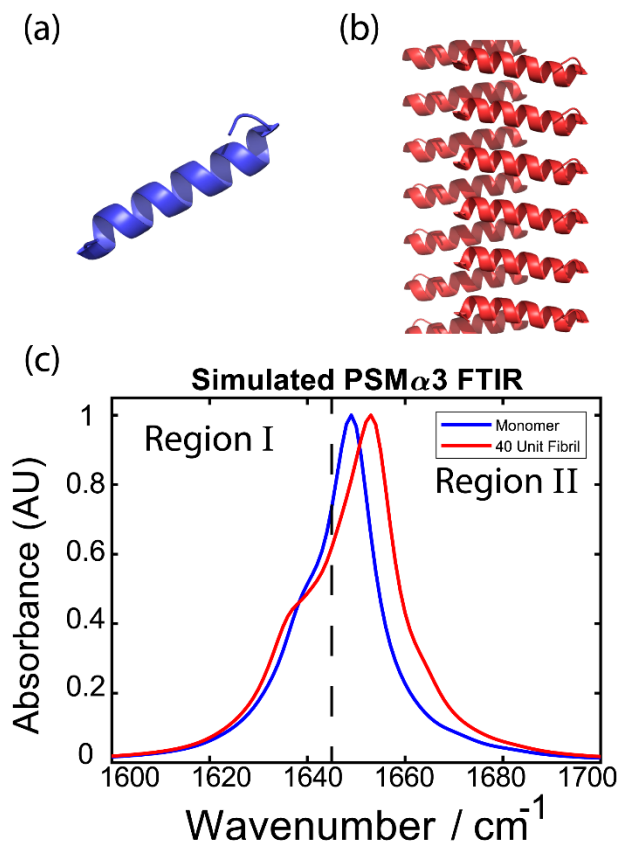

FIG. 1. PDB structures of PSMα3 monomers (a) and fibers (b) extended along the screw-axis. (c) Simulated FTIR spectra of PSMα3 monomers and fibers without diagonal disorder.

We chose to divide the spectra into two regions split at 1645 cm^{-1} where the higher frequency region contains the main peak and the lower region contains the shoulder which we then perform the doorway mode analysis on. For the monomer, the strongest doorway mode within the higher frequency region appears to have a strong A mode character (Fig 2b). In the region below 1645 cm^{-1}, the two strongest doorway modes shown in Figure 2a are both E_1-like modes which shows the overall FTIR peak structure for PSMα3 monomer conforms with that of idealizes α-helices.
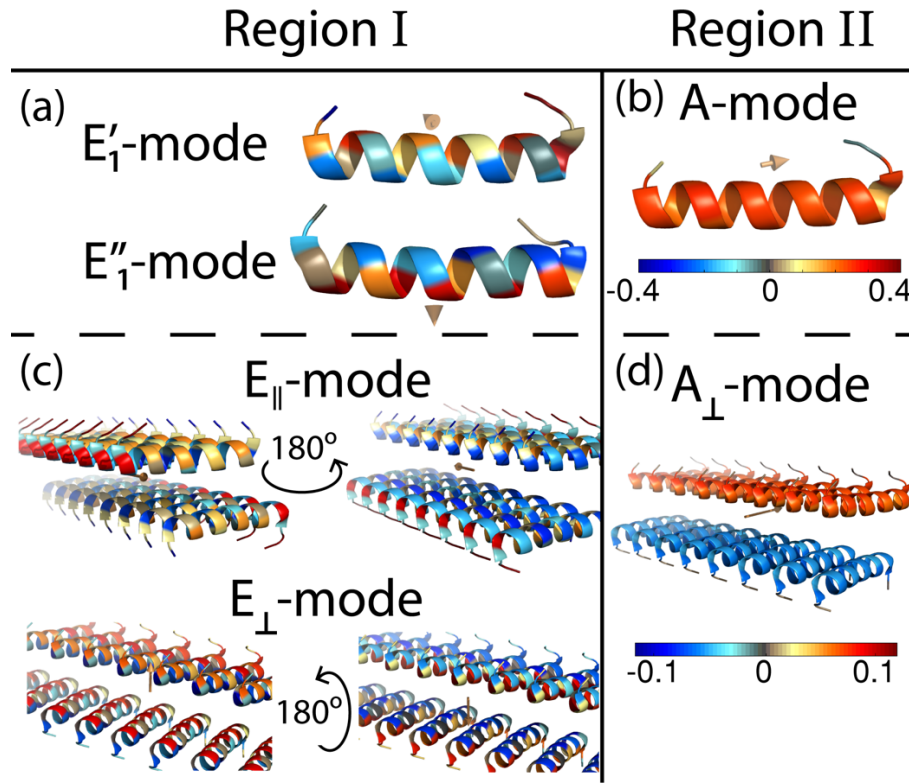
FIG. 2. Doorway mode analysis on the spectra shown in Figure 1. Doorway mode analysis shows the most prominent modes for both the monomer and fiber in the specified regions below and above 1645 cm^{-1}, along with transition dipole vectors (a) and (b) show the E-like and A-like doorway modes for the monomer, respectively. (c) and (d) show the E-like and A-like modes for the fiber, respectively. The color bar shows the amplitude and phase of each residue for each mode.

Applying the doorway analysis on the fibril structure spectrum, the PSMα3 fibril structure's strongest doorway mode above 1645 cm^{-1}, shown in Fig 2d, is characterized by stacks of α-helical A-modes, where the two sheets that make up the fibril have opposite phase to one another. As the two sheets of helices have opposite orientations, the total transition dipole moment for both sheets are in the same direction resulting in a strong overall transition dipole moment that is perpendicular the fibril screw axis. This extended A-like mode clearly results from coupling between helical subunits. We designate this mode $A_\perp$ to indicate that the transition dipole is perpendicular to the fibril axis. Figure 2c shows that for the region below 1645 cm^{-1}, the 2 brightest states have an E_1 character, one of which has a transition moment that runs parallel to the fibril axis. We designate this mode $E_\parallel$, to indicate that its transition moment is parallel to the fibril axis. The other has a transition moment that is perpendicular to the other two, which we designate $E_\perp$. The expectation values for the energy of these modes, using $A_\perp$ as an example, is calculated as $\langle A_\perp | \hat{H} | A_\perp \rangle$, where $\hat{H}$ is the system Hamiltonian defined in Eq. A5 and $|A_\perp\rangle$ is the doorway mode in the local mode basis. We found this expected energy value to be equal to 1653 cm^{-1} for $A_\perp$, 1646 cm^{-1} for $E_\perp$, and 1642 cm^{-1} for $E_\parallel$.

We turn to 2DIR calculations to further investigate the inter-helix vibrational coupling, as 2DIR is especially sensitive to coupling.[31] Although expected shifts in frequencies due to intramolecular interactions between the localized A and E_1 modes are small, the effects of coupling can be teased out of 2DIR measurements using the polarization sensitivity of cross peaks. It is important to note that the transition dipoles of the extended $A_\perp$, $E_\parallel$, and $E_\perp$ modes are very nearly perpendicular to one another, making polarization well-suited for this analysis. We simulated polarization dependent 2DIR measurements to isolate cross-peaks in the spectrum and probe relative orientation between transition moments. This can be used to isolate cross peaks even from nearly degenerate vibrational modes.[28,32,33]

The diagonal peak signals in the XXXX (i.e., pump-probe parallel polarization) are three times larger than the diagonal peaks in the XXYY (pump-probe perpendicular) signal. The ratio between the cross-peak signals in the XXXX and XXYY polarizations, however, depends on the angle between the modes and the polarization of incident light. The ability to select out different pathways through polarization control is important as it can allow us to remove diagonal contributions from the spectrum.[34,35] Because the frequency splitting between A and E_1 modes in α-helices is relatively small, peaks along the diagonal obscure cross-peaks. By calculating polarization difference spectra, we can eliminate these obscuring signals.
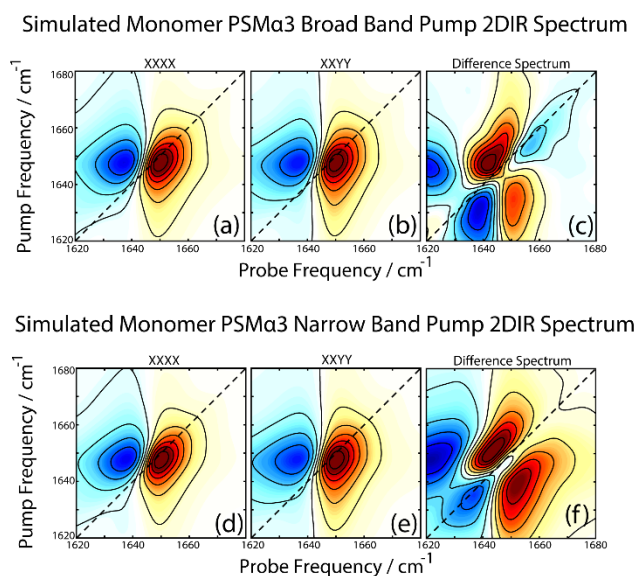

FIG. 3. Simulated 2DIR spectra of monomeric PSMα3 using broad band (top) and narrow band (bottom) pump conditions. The XXXX, XXYY, and difference spectrum was calculated for each. The difference spectra reveal cross-peaks consistent with the A and E mode coupling of α-helices.

Figure 3a and b shows simulated 2DIR spectra of monomeric PSMα3 for XXXX and XXYY polarizations, respectively. The spectra agree well with the 2DIR spectrum for a purely α-helical peptide, such as the spectrum in Figure 1d of reference 28.[28] We normalized both spectra to their peak amplitude then subtracted the parallel signal from the perpendicular. Figure 3c

shows the simulated difference spectrum, displaying what appears to be two cross peak pairs at pump frequencies 1635 and

1647 cm^{-1}, close to the frequencies for the α-helix A and E_1 modes, respectively.[16]
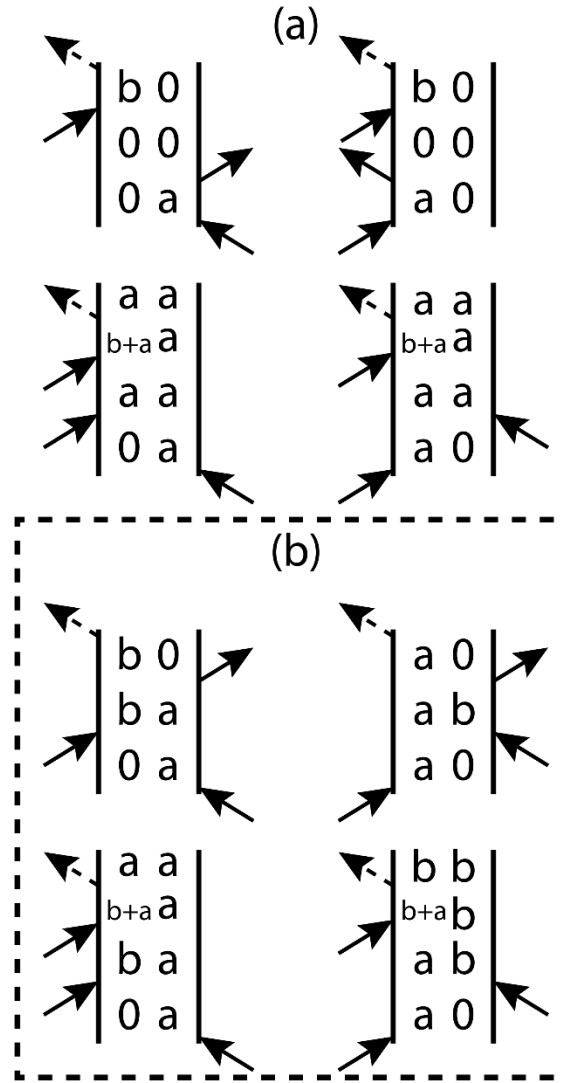

FIG. 4. Double-Sided Feynman diagrams showing all possible cross-peak pathways. The first four pathways (a) are allowed in the narrow band experiment and come in rephasing and non-rephasing pairs, leading to absorptive features in the spectra whereas the four pathways in the box (b) are not allowed in the narrow band experiment, and all lack a phase conjugate partner, leading to non-absorptive features. All eight pathways are allowed in the broad band experiment.

By calculating all Feynman pathways, as featured in Figure 4, though, we have implicitly calculated the broad band pump

version of the 2DIR experiment, as we allow for the excitation of two excitons with two different frequencies during the pump

interactions. It is sometimes convenient, however, to collect 2D spectra using a narrow band pump where the first two

interactions occur at the same (or similar) frequencies. This restricts the set of pathways sampled only to those where there is

no coherent state during the waiting time, T_2, eliminating non-absorptive cross-peak features, some of which lie along the

diagonal. This reduces the overall complexity of the 2DIR spectrum while still retaining much of the useful cross-peak

information 2DIR provides.[36] Figures 3d-f show the spectra for the monomer using this narrow band approach. While the

polarization control simulations remain almost identical to their broad band pump counterparts, cross-peak pair identification is easier using the narrow band approach. Similar peak pairs have been reported for narrow band pump 2DIR measurement of model helical peptides.[28,37,38]
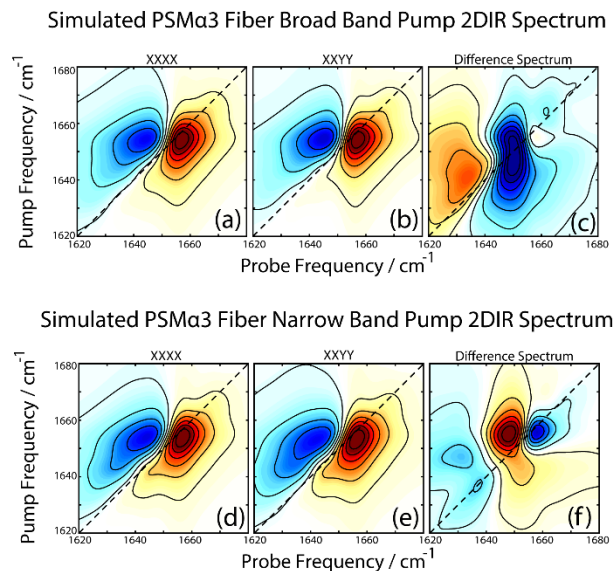

FIG. 5. Simulated 2DIR spectra of PSMα3 fibers extended 20-unit cells (40 peptides) along the screw-axis using broad band (top) and narrow band (bottom) pump conditions. The narrow band difference spectrum has a similar cross-peak pattern to that of the monomer whereas the broad-band spectrum has a new peak pattern along the diagonal.

We also applied this method on a 20-unit cell (40 peptide) PSMα3 fibril structure. The Figures 5a-c show the spectra using the broad band approach. The difference spectrum displays a set of peaks with no clear peak pairs. The change between Figures 3c and 5c indicates that fibril formation has some effect on the spectrum, but it is unclear where the change originates from, though overall appearance is that of a non-rephasing signal on the diagonal, which may result from "diagonal" cross peaks pathways of the sort seen in the right column of Figure 4b. Additionally, we also performed simulations using the narrow band approximation shown in Figures 5d-f. This difference spectrum shows the return of the A and E_1 coupled cross-peaks, though with differing peak ratios compared to the monomer. The difference between the broad band and narrow band difference spectra suggest that new diagonal coherent cross-peaks in the spectra result from coherent coupling between the fibril modes.

Simulated PSMα3 Broad Band Pump 2DIR Spectra with Increasing Fiber Length

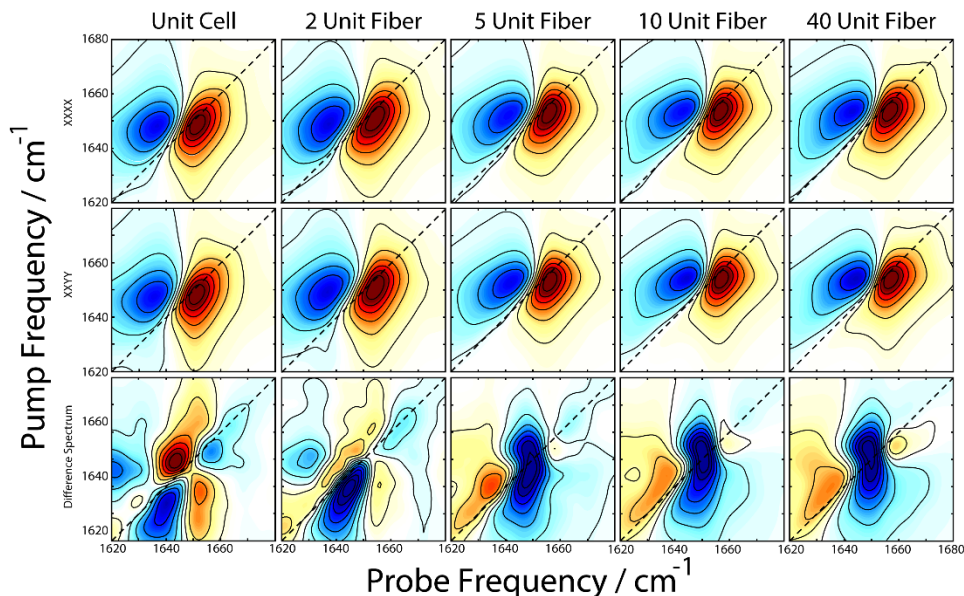FIG. 6. Simulated PSMα3 calculated using XXXX and XXYY polarizations with increasing fiber lengths. The bottom row displays the difference spectra for all fiber lengths. As more units are added, the center blue vertical shaped peak becomes more prominent.

To test whether the cross-peak pattern in Figure 5c arose due to through-fibril interactions, we simulated the 2DIR spectra with increasing length of PSMα3 fibril, starting with a single unit cell consisting of two repeats of the peptide, to a 40-unit cell fibril consisting of 80 peptide repeats. The simulation results in Figure 6 show that the main diagonal peaks in the XXXX spectra remain mostly unchanged with increasing fiber length, but the underlying cross-peaks seen in the difference spectra gradually shifts from the pattern seen for the monomer in Figure 3c to a peak pattern consistent with the non-rephasing 2DIR lineshape pattern of the fibril, which would be expected from coherent cross-peaks arising from interactions along the fibril axis.[35]
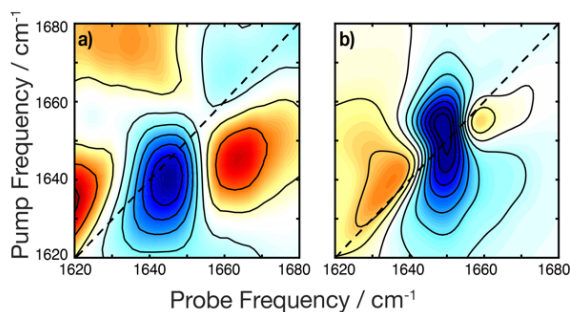

FIG. 7. Comparison of (a) experimental 2DIR difference spectrum of PSMα3 fibers[39] vs (b) simulated 2DIR difference spectrum of a 40 unit fiber PSMα3.

Our previous study examining the experimental 2DIR spectra of PSMα3 fibers produced a polarization difference spectrum (Figure 7a) that agrees with our simulated difference spectrum in Figure 7b. The long vertical blue peak appears to result from the coupling of modes within the fibril state.

B. Molecular origin of the characteristic cross-α signal

To explore the molecular origin of the coherent peaks along the diagonal that appear to be characteristic of cross-α structures, we simulated the spectrum of a 5-unit fiber without diagonal disorder, filtering out any peaks which did not contribute to a coherent signal. Specifically, when calculating the rephasing signal, rather than summing over all combinations of $e_4 e_3 e_2 e_1$ in Eqs. C8, we included only contributions where $e_1 = e_3$, $e_2 = e_4$, and $e_1 \neq e_2$. Likewise, when calculating the non-rephasing spectrum, the sum included only contributions where $e_1 = e_4$, $e_2 = e_3$, and $e_1 \neq e_2$. This filtered coherent-only spectrum allowed us to determine the normal modes responsible for the coherent signal along the diagonal of the cross-polarization difference spectrum. For simplicity, we refer to the mode that undergoes the first interaction, e_1, as mode a and the mode that undergoes the second interaction, e_2, as mode b. The effect of these filtering conditions is that we only sum over pathways which involve a coherence along T_2, corresponding to the Feynman diagrams shown in Figure 8. The range of coherence frequencies, $|\omega_a - \omega_b|$, was limited to 2 to 16 cm^{-1} to ensure that any coherences between the $A_\perp$, $E_\parallel$, and $E_\perp$ modes were captured, as the differences in their expected energy values, reported in section III.A above, fall in this range.
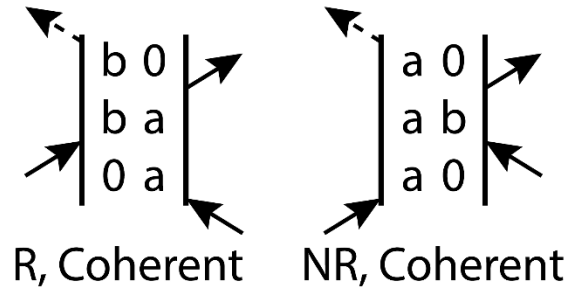

FIG. 8. Feynman diagrams showing both rephasing and non-rephasing coherent pathways. These pathways undergo oscillations of $|\omega_a - \omega_b|$ during T_2.
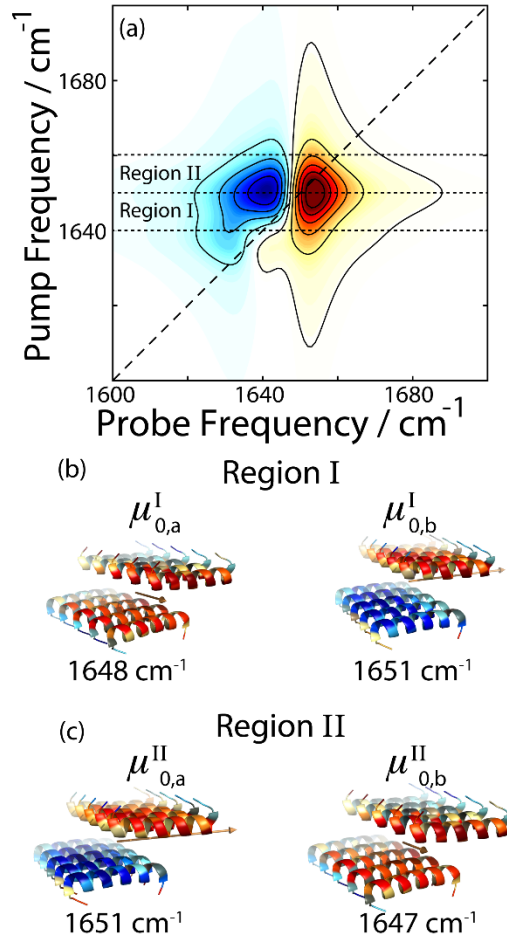
FIG. 9. (a) Filtered, coherence-only spectrum, as described in the main text, calculated from coherent signals where the difference frequency between the two modes is 2 to 8 cm^{-1}. (b) The first doorway mode calculated using the coupled transition dipoles in region I. $\mu_{0,a}^{I}$ is the doorway state from the transition dipoles calculated from the first excited mode whereas $\mu_{0,b}^{I}$ is the transition dipole calculated from the second excited mode. (c) The first doorway modes of all pairs of coupled modes in region II.

In Figure 9a, we plotted the filtered coherence-only spectrum where $2 \leq |\omega_a - \omega_b| < 8$ cm^{-1}. The choice of a cutoff of 8 cm^{-1} was motivated by the expectation values found above for the extended modes $A_\perp$ (1653 cm^{-1}), $E_\perp$ (1646 cm^{-1}), and $E_\parallel$ (1642 cm^{-1}), as we expected coherences between $A_\perp$ and $E_\perp$ to lie in this region, and coherences between $A_\perp$ and $E_\parallel$ to lie in the 8-16 cm^{-1} range, which is plotted in Figure 10. The coupling between modes is obscured in these diagonal cross peaks due to the signal resonating at the same frequency, ω_a, during both τ_1 and τ_3. Typically, one could perform a waiting time study along T_2 to determine the difference frequency between ω_a and ω_b and thus backtrack to determine the coupled modes. Here, however, we can determine the coupled modes directly by keeping a list of all pairs of modes a and b that contribute to this signal and doing doorway analysis on the two sets of transition moments, $\{\mu_a\}$ and $\{\mu_b\}$. In Figure 9b, we present the brightest a and b doorway modes from the region of the spectrum from 1640 to 1650 cm^{-1} and map the resulting amplitudes and phases

of the doorway modes onto the crystal structure. This analysis reveals that the signal in Region I of the filtered coherent spectrum in Figure 9a original form coupling between the $A_\perp$ and $E_\parallel$ modes. Repeating the doorway analysis on the region from 1650 to 1660 cm⁻¹, shown in Figure 9c, gives similar doorway modes in reverse order.
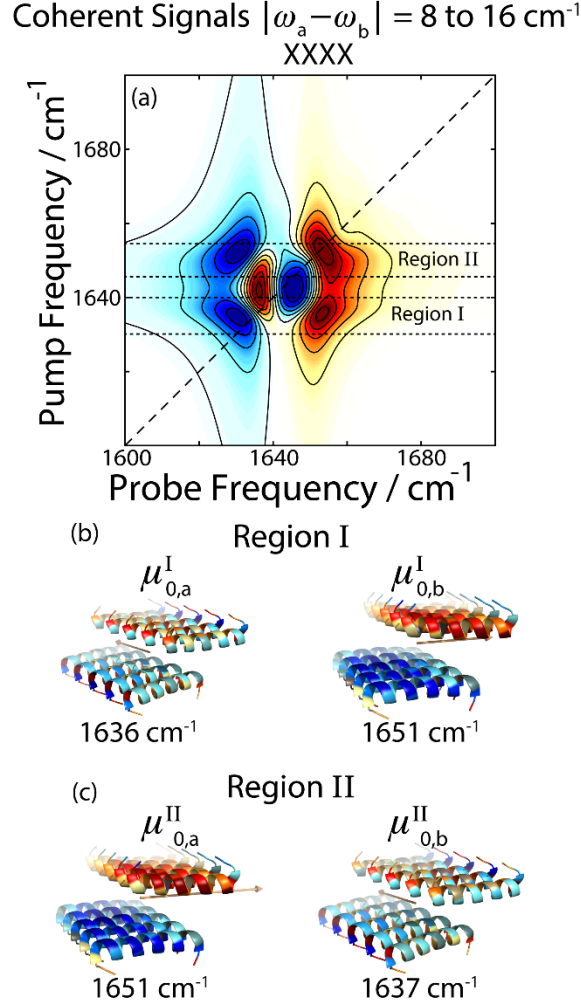

FIG. 10. (a) Filtered, coherence-only spectrum calculated from coherent signals where the difference frequency between the two modes is 8 to 16 cm⁻¹. (b) The first doorway mode calculated using the coupled transition dipoles in region I. $\mu^I_{0,a}$ is the doorway state from the transition dipoles calculated from the first excited mode whereas $\mu^I_{0,b}$ is the transition dipole calculated from the second excited mode. (c) The first doorway modes of all pairs of coupled modes in region II.

Repeating the calculations for interactions where $8 \leq |\omega_a - \omega_b| < 16$ cm⁻¹ revealed a new peak pattern in Figure 10a. The doorway mode analysis of the first and second excitations as described above were repeated and the results plotted in Figure 10b and c, from which it can be seen that the origin of these peaks is also coupling between $A_\perp$ and $E_\parallel$ modes. No evidence of coherent signal originating from coupling to the $E_\perp$ was found. It's possible that such an interaction would be forbidden for symmetry reasons, though this would require further theoretical efforts in the future. The present analysis does

support the view, though, that interactions between the newly formed delocalized states in the cross-α structure lead to the diagonal signature in Figure 7.

C. Time dependence of diagonal coherences

Because the $A_\perp$ and $E_\parallel$ modes of the fibril appear to be coherently coupled, we should expect the coherent diagonal cross-peaks to oscillate along the T_2 axis. We performed simulations of the 8-unit fiber with waiting times ranging from 0 to 5 ps in 0.5 ps increments. The difference spectra for select timepoints are plotted in Figure 11a. The diagonal cross-peaks evolve with increasing waiting times which is what we would expect for coherent cross-peaks. During early time points, the difference spectrum is dominated by contributions along the diagonal. The later timepoints, however, are almost completely dominated by static cross-peaks and the difference spectrum effectively appears like the monomer difference spectrum. This rapid loss of coherent signals can be explained by the fact the $A_\perp$ and $E_\parallel$ modes are each really a superposition of closely spaced but non-degenerate energy eigenstates, the frequencies of which quickly go out of phase with one another, leaving behind only static cross peaks.
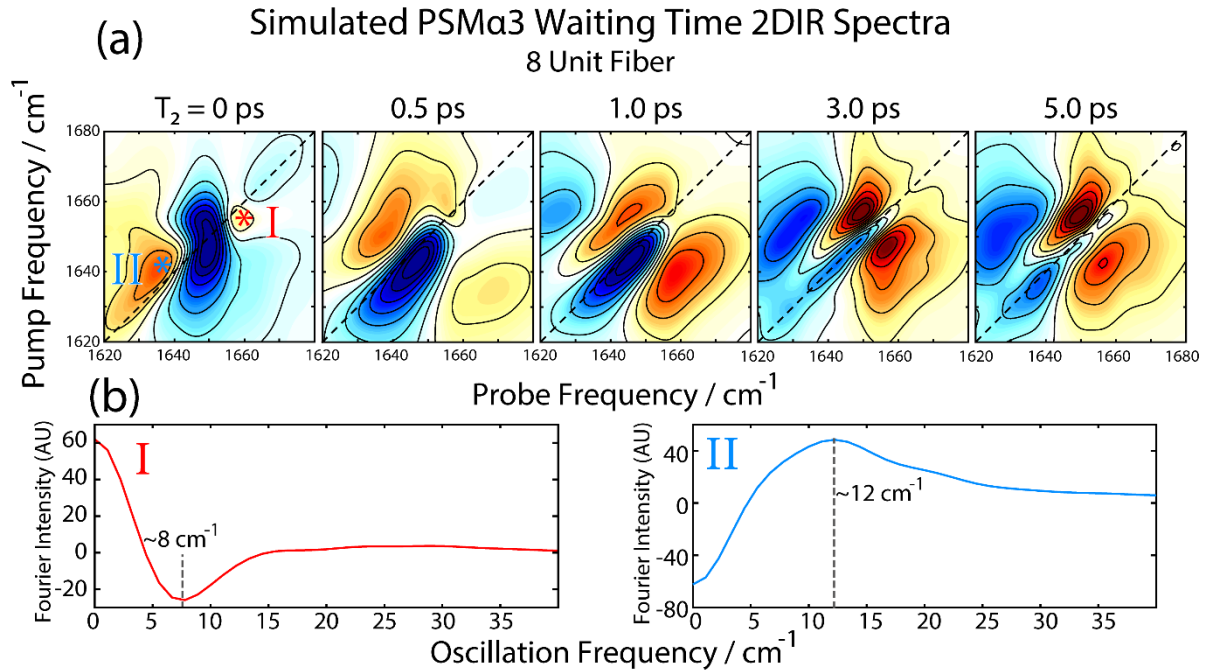

FIG. 11. (a) Simulated difference spectra of an 8-unit fiber calculated at the indicated T_2 waiting times. (b) Fourier transforms of two slices of the spectrum, sliced through the indicated pixels along the T_2 dimension.

To pick out the coherence frequency along T_2, we picked two points from the spectra and took a slice of those points along the T_2 axis. We performed Fourier transformation of the slice to determine the oscillation frequencies present, similar to what has been done to extract coherence frequencies in Two-Dimensional Electronic Spectroscopy (2DES).[40] Figure 11b shows the Fourier transforms for two slices taken at the indicated points. The spectrum for the slice taken from the point I at about

1655 cm^{-1} on the pump axis is weakly peaked at around 8 cm^{-1}, while the spectrum generated from point II is peaked near 12 cm^{-1}. These values roughly agree with the differences between expected energy values for the doorway states $A_\perp$, $E_\perp$ and $E_\parallel$.

IV. DISCUSSION

The sets of simulation methods we performed all point to the emergence of a characteristic coherent cross-peak signal of PSMα3 cross-α fibers, emerging from interactions between newly formed extended modes of the fibrils. Analyzing differences between narrow -band and broad-band spectra can allow one to discriminate between coherent signals in the 2DIR spectrum. Furthermore, we can determine the source of the coherences in simulations directly through filtering out non-coherent signals and examining the modes responsible for the remaining signal. Using waiting time simulations, we can confirm the frequencies of the coherent oscillations in the signal are correlated to the coupled modes we determined previously.

The shape of the coherent cross-peaks appearing in the polarization difference spectra of cross-α fibrils is that of a non-rephasing lineshape. The non-rephasing origin of the peaks causes the three lobed structure seen in Figure 7b. Generally, coherent cross-peaks arising from rephasing pathways will dominate the off diagonal regions of polarization difference 2DIR spectrum, while non-rephasing coherent cross-peaks dominate the diagonal regions.[35] The appearance of the strong non-rephasing signal along the diagonal of the spectra in Figure 7 is thus not surprising.

Deep analysis on the origin of coherent peaks has been sparse within the 2DIR community, limited to small molecules and localized sites where there are a handful of total pathways to consider.[41,42] Analysis of cross-peaks and differences between rephasing and non-rephasing spectra, however, has been closely explored in 2DES, especially in the case of supra-molecular light harvesting systems, where examination of quantum beating and non-rephasing signals have been used to determine mechanism of energy transfer and relaxation in congested spectra.[43–45] For example, many 2DES studies have leveraged details of the coherences in light harvesting complexes to determine that long lived quantum beats have vibrational origins.[46–48] In another study involving artificial light harvesters aligned via a wire guide exhibits quantum beating as well as a more intense non-rephasing peak compared to the rephasing peak.[49] Here, we have employed methods similar in spirit to determine the molecular origin of 2DIR signals of cross-α fibrils. We have shown it is possible to obtain insights into the vibrational coherences in super-molecular structures and that careful examination of these coherent peaks may prove to be useful in resolving super-molecular structure in the future.

V. CONCLUSION

In conclusion, we have used variety of IR spectrum simulation techniques to decode the infrared spectra of cross-α fibrils, a structure with many oscillators and a relatively featureless FTIR and absorptive 2DIR spectrum. We simulated both narrowband and broadband polarization selective 2DIR spectra of PSMα3 fibers using the nonlinear exciton scattering

simulation approach. We identified three new characteristic extended vibrational exciton states characteristic of cross-α, the $A_\perp$, $E_\perp$, and $E_\parallel$ modes. We also showed that a combination of polarization selectivity and narrowband/broadband spectra allowed us to identify and characterize a coherent cross peak between these new modes that is characteristic of cross-α fibrils. We believe that chracterization of this signature may allow future identifications of cross-α structure in solution phase measurements. We also believe that the approach presented, combining polarization selectivity, time and frequency domain measurements, and doorway state analysis, can be a fruitful strategy for investigating molecular origins for congested spectra of other supramolecular complexes.

VI. APPENDIX

A. One-quantum site-energy model

The Hamiltonian $\widehat{H}$ for a quantum system can be written as

$$\widehat{H} = \widehat{H}_0 + \widehat{H}', \tag{A1}$$

where $\widehat{H}_0$ is the Hamiltonian of the molecular aggregate and $\widehat{H}'$ describes the interactions between the molecules and the light. For a molecular aggregate with energy levels ε_e and eigenstates $|\psi_e\rangle$, the time independent Schrodinger equation is

$$\widehat{H}_0|\psi_e\rangle = \varepsilon_e|\psi_e\rangle. \tag{A2}$$

The external electric field $\boldsymbol{E}(t)$ of the light pulses in the 2D experiment acts on the system through the dipole operator $\widehat{\boldsymbol{\mu}}$,

$$\widehat{H}'(t) = -\widehat{\boldsymbol{\mu}} \cdot \boldsymbol{E}(t). \tag{A3}$$

The dipole operator takes a vibrational mode up or down an energy level

$$\widehat{\boldsymbol{\mu}} = \sum_m (b_m^\dagger + b_m) \, \boldsymbol{\mu}_m, \tag{A4}$$

where $b_m^\dagger$ and b_m are the creation and annihilation operators for local mode m, respectively, and $\boldsymbol{\mu}_m$ is the transition dipole moment of local mode m. The full Hamiltonian can be written in the local mode basis as

$$\widehat{H}(t) = \sum_{m,n} \delta_{mn}\varepsilon_m b_m^\dagger b_m + (1 - \delta_{mn})\beta_{mn} b_m^\dagger b_n - \sum_m (b_m^\dagger + b_m) \, \boldsymbol{\mu}_m \cdot \boldsymbol{E}(t), \tag{A5}$$

where ε_m is the energy of local mode m and β_{mn} is the coupling energy between local modes m and n.

To obtain the local mode frequencies, we modeled each amide bond in the structure as a floating oscillator and assigned it a frequency of 1650 cm^{-1} plus a random offset, to produce gaussian diagonal disorder, to model the frequency of a free amide-

I mode. We made use of a transition dipole coupling (TDC) model to calculate the coupling energies between each local mode. Here, the coupling energies are calculated as

$$\beta_{mn} = \frac{|\mu|^2}{4\pi\epsilon_0}\left[\frac{\hat{\mu}_m\cdot\hat{\mu}_n - 3(\hat{r}_{mn}\cdot\hat{\mu}_m)(\hat{r}_{mn}\cdot\hat{\mu}_n)}{r_{mn}^3}\right], \tag{A6}$$

where $|\mu|$ is the strength of an amide-I transition dipole moment, ϵ_0 is the vacuum permittivity, $\hat{\mu}_m$ is the unit vector describing the orientation of transition dipole m, $\hat{r}_{mn}$ is the unit vector of the separation between μ_m and μ_n, and r_{mn} is the distance between μ_m and μ_n.

Diagonalization of $\hat{H}$ gave the energies of the exciton modes ε_e as well as their associated eigenvectors ψ_e. Written in matrix notation, this looks like

$$H = \sum_e|\psi_e\rangle\varepsilon_e\langle\psi_e|. \tag{A7}$$

We obtained the excitonic transition dipole moment μ_e which describe the strength and orientation of an excitonic modes in the system by

$$\mu_e = \sum_m^N \psi_{e,m}\mu_m, \tag{A8}$$

where $\psi_{e,m}$ are the expansion coefficients of the exciton states, $|\psi_e\rangle$, in the local mode basis. The linear absorbance spectra were calculated by summing stick spectra on a frequency grid according to the mode frequency, ω_e, scaled by the transition dipole strength of the mode. Stick spectrum were then convolved with a Lorentzian lineshape to give the final spectra, according to

$$I(\omega) = \sum_e|\mu_e|^2 \times \delta\big(round(\omega - \omega_e)\big) \otimes \text{IM}\left(\frac{-1}{\omega+i\gamma}\right). \tag{A9}$$

B. Doorway state model

Following the methods of Tokmakoff, we used Singular Value Decomposition (SVD) to decompose regions of the spectra with densely packed states into three orthogonal bright doorway modes which gives an overall representation of the origin of the signal.[18] The set of excitonic transition dipoles within the spectral regions is first obtained by selecting a subset of ψ_e whose associated energies fall within this region of interest

$$\tilde{\mu}_e^{sub} = {}_{sub}\Psi_e^\dagger\tilde{\mu}_m. \tag{B1}$$

Here we define $\widetilde{\boldsymbol{\mu}}_m$ as the N×3 matrix whose rows are the local transition dipoles $\boldsymbol{\mu}_m$ and columns are the components of those vectors. Similarly, $\widetilde{\boldsymbol{\mu}}_e^{sub}$ is a n×3 matrix whose rows are the subset of exciton transition dipoles and columns are the components of the vectors. The matrix $_{sub}\Psi_e$ is an N×n matrix which contains the subset of ψ_e eigenvectors in its columns.

Next, matrix SVD is performed on $\widetilde{\boldsymbol{\mu}}_e^{sub}$ to generate the decomposition:

$$\widetilde{\boldsymbol{\mu}}_e^{sub} = U_{sub}S_{sub}V_{sub}^T, \tag{B2}$$

where S_{sub} is the diagonal matrix of singular values of the matrix $\widetilde{\boldsymbol{\mu}}_e^{sub}$ and V_{sub}^T is the 3×3 matrix of the transition dipole moments for three bright doorway modes. U_{sub} is the transformation matrix which builds $\widetilde{\boldsymbol{\mu}}_e^{sub}$ from the underlying doorway mode basis set.[17] Thus we define $\widetilde{\boldsymbol{\mu}}_d^{sub}$ as the matrix of representative transition dipole moments of the spectral region referred to as the doorway transition dipoles,

$$\widetilde{\boldsymbol{\mu}}_d^{sub} \equiv S_{sub}V_{sub}^T. \tag{B3}$$

This can be rewritten using U_{sub} as the transformation matrix between $\widetilde{\boldsymbol{\mu}}_e^{sub}$ and $\widetilde{\boldsymbol{\mu}}_d^{sub}$ as

$$\widetilde{\boldsymbol{\mu}}_d^{sub} = U_{sub}^T\widetilde{\boldsymbol{\mu}}_e^{sub}. \tag{B4}$$

We can then relate the contributions to the doorway transition dipoles back to local transition dipoles of the structure through the transformation matrix and the eigenvectors of the modes,

$$\widetilde{\boldsymbol{\mu}}_d^{sub} = \Phi_{sub}^T\widetilde{\boldsymbol{\mu}}_m, \tag{B5}$$

where $\Phi_{sub} = {}_{sub}\Psi_e U_{sub}$. The columns of Φ_{sub} give the amplitude and phase of the contribution of each local transition to the doorway mode. We applied the amplitudes and phases in Φ_{sub} back onto the local modes to plot the doorway modes in the main text. To obtain an average energy for the doorway mode, we used the transformation matrix U_{sub} which gives the contribution of each excitonic transition dipole to the doorway mode. We used the amplitude squared of the transformation matrix, U_{sub}^2, to weight the contribution of each exciton mode to the spectrum which we used to assign an average energy to each doorway mode,

$$\varepsilon_d^{sub} = \sum_e U_{sub_{e,d}}^2 \varepsilon_e^{sub}. \tag{B6}$$

C. Nonlinear exciton scattering model

The third-order response is obtained through the nonlinear exciton scattering model detailed by Mukamel and others.[20,50,51] Starting with Eq. (A5), we included an additional term which acts like a quartic expansion of an anharmonic potential,

$$\hat{H} = \sum_{m,n} \delta_{mn}\varepsilon_m b_m^\dagger b_m + (1 - \delta_{mn})\beta_{mn}b_m^\dagger b_n \tag{C1}$$

$$+\sum_{mn,pq} \mathbb{U}_{mn,pq} b_m^\dagger b_n^\dagger b_p b_q - \sum_m \left(b_m^\dagger + b_m\right) \boldsymbol{\mu}_m \cdot \boldsymbol{E}(t),$$

where $\mathbb{U}_{mn,pq} = \frac{\Delta}{4}\left(\delta_{mp}\delta_{nq} + \delta_{mq}\delta_{np}\right)$ and Δ is the site anharmonic shift.

The third-order polarization can be calculated for the rephasing ($k_R = -k_1 + k_2 + k_3$) and non-rephasing ($k_{NR} = +k_1 - k_2 + k_3$) signals,

$$P_{\nu_4}^{k_R}(\tau_3, T_2, \tau_1) = \frac{1}{2^3}\exp\left(+i\phi_3 + i\phi_2 - i\phi_1\right)\sum_{\nu_3\nu_2\nu_1} S_{\nu_4\nu_3\nu_2\nu_1}^{k_R}(\tau_3, T_2, \tau_1)E_{\nu_3}E_{\nu_2}E_{\nu_1} \qquad (C2)$$

and

$$P_{\nu_4}^{k_{NR}}(\tau_3, T_2, \tau_1) = \frac{1}{2^3}\exp\left(+i\phi_3 - i\phi_2 + i\phi_1\right)\sum_{\nu_3\nu_2\nu_1} S_{\nu_4\nu_3\nu_2\nu_1}^{k_{NR}}(\tau_3, T_2, \tau_1)E_{\nu_3}E_{\nu_2}E_{\nu_1}. \qquad (C3)$$

Here, $P_{\nu_4}^{k_R}$ and $P_{\nu_4}^{k_{NR}}$ are the third order polarizations for the rephasing and non-rephasing diagrams, ϕ_i are the phases of the ith pulses, $S_{\nu_4\nu_3\nu_2\nu_1}^{k_R}$ and $S_{\nu_4\nu_3\nu_2\nu_1}^{k_{NR}}$ are the non-linear response functions for the rephasing and non-rephasing diagrams, and E_{ν_i} are the electric fields, and ν_i are used to donate the polarization of the ith light interaction. The non-linear response functions depend on the wavevectors and the time intervals ($\tau_3 = t_4 - t_3, T_2 = t_3 - t_2, \tau_1 = t_2 - t_1$) between pulses. The non-linear response function is obtained through propagating multiple excitations in the one-quantum exciton manifold. These responses are defined in terms of Green functions, which describe the forward propagation of under the influence of the Hamiltonian. The time-domain Green function is

$$G(t) = \theta(t)\exp\left(-\frac{i}{\hbar}H(t)\right), \qquad (C4)$$

where $\theta(t)$ is the Heaviside step function ($\theta(t) = 0$ for $t < 0$, $\theta(t) = 1$ for $t \geq 0$).

The Green function for each site can be calculated by transforming the excitonic Green function into the individual site basis,

$$G_{m,n}(t) = \sum_e \psi_{em} I_e(t)\psi_{en}^*, \qquad (C5)$$

where the excitonic Green function gives the propagation of an excitation into an exciton mode,

$$I_e(t) = \theta(t)\exp(-i\varepsilon_e t - \gamma_e t), \qquad (C6)$$

where γ_e is the dephasing rate for exciton e.

Tracking the propagation of each exciton excitation over each time interval where the excitation exists gives the non-linear response. The inclusion of the exciton scattering matrix $\Gamma_{e_4 e_3, e_2 e_1}$ allows for the interaction between excitations which allows for the non-linear signals to appear. The scattering is integrated over all possible mixing times giving a response of

$$S^k_{v_4 v_3 v_2 v_1}(\tau_3, T_2, \tau_1) = 2i \sum_{e_4 e_3 e_2 e_1} M^{v_4 v_3 v_2 v_1}_{e_4 e_3 e_2 e_1} \times \int_0^{\tau_3 + T_2} d\tau_s'' \int_0^{\tau_s''} d\tau_s' \, I_{e_4}(\tau_s') \times \\ I^*_{e_3}(\tau_3 + T_2 + \tau_1 - \tau_s') \Gamma_{e_4 e_3, e_2 e_1}(\tau_s'' - \tau_s') I_{e_2}(\tau_3 + T_2 - \tau_s'') I_{e_1}(\tau_1 - \tau_s'').$$

(C7)

Applying the time ordering of the pulses for the rephasing and non-rephasing signals gives,

$$S^{k_R}_{v_4 v_3 v_2 v_1}(\tau_3, T_2, \tau_1) = 2i \sum_{e_4 e_3 e_2 e_1} M^{v_4 v_3 v_2 v_1}_{e_4 e_3 e_2 e_1} \times \int_0^{\tau_3} d\tau_s'' \int_0^{\tau_s''} d\tau_s' \, I_{e_4}(\tau_s') I^*_{e_1}(\tau_3 + T_2 + \tau_1 - \tau_s') \times \\ \Gamma_{e_4 e_1, e_3 e_2}(\tau_s'' - \tau_s') I_{e_3}(\tau_3 - \tau_s'') I_{e_2}(\tau_3 + T_2 - \tau_s'')$$

(C8)

and

$$S^{k_{NR}}_{v_4 v_3 v_2 v_1}(\tau_3, T_2, \tau_1) = 2i \sum_{e_4 e_3 e_2 e_1} M^{v_4 v_3 v_2 v_1}_{e_4 e_3 e_2 e_1} \times \int_0^{\tau_3} d\tau_s'' \int_0^{\tau_s''} d\tau_s' \, I_{e_4}(\tau_s') I^*_{e_2}(\tau_3 + T_2 - \tau_s') \times \\ \Gamma_{e_4 e_2, e_3 e_1}(\tau_s'' - \tau_s') I_{e_3}(\tau_3 - \tau_s'') I_{e_1}(\tau_3 + T_2 + \tau_1 - \tau_s'').$$

(C9)

$M^{v_4 v_3 v_2 v_1}_{e_4 e_3 e_2 e_1}$ is defined as the orientationally averaged transition dipole strengths between the four local modes,

$$M^{v_4 v_3 v_2 v_1}_{e_4 e_3 e_2 e_1} \equiv \langle (\boldsymbol{\mu}_{e_4} \cdot \widehat{\boldsymbol{E}}_{v_4})(\boldsymbol{\mu}_{e_3} \cdot \widehat{\boldsymbol{E}}_{v_3})(\boldsymbol{\mu}_{e_2} \cdot \widehat{\boldsymbol{E}}_{v_2})(\boldsymbol{\mu}_{e_1} \cdot \widehat{\boldsymbol{E}}_{v_1}) \rangle$$

(C10)

which we calculate using[35]

$$M^{v_4 v_3 v_2 v_1}_{e_4 e_3 e_2 e_1} = \frac{1}{30} |\mu_{e_4}||\mu_{e_3}||\mu_{e_2}||\mu_{e_1}| \begin{pmatrix} cos\theta_{v_1 v_2} cos\theta_{v_3 v_4} \\ cos\theta_{v_1 v_3} cos\theta_{v_2 v_4} \\ cos\theta_{v_1 v_4} cos\theta_{v_2 v_3} \end{pmatrix}^T \begin{pmatrix} 4 & -1 & -1 \\ -1 & 4 & -1 \\ -1 & -1 & 4 \end{pmatrix} \begin{pmatrix} cos\theta_{e_1 e_2} cos\theta_{e_3 e_4} \\ cos\theta_{e_1 e_3} cos\theta_{e_2 e_4} \\ cos\theta_{e_1 e_4} cos\theta_{e_2 e_3} \end{pmatrix},$$

(C11)

where $cos\theta_{v_i v_j}$ describes the cosine of the angle between polarizations of light pulses $\widehat{\boldsymbol{E}}_{v_i}$ and $\widehat{\boldsymbol{E}}_{v_j}$, and $cos\theta_{e_i e_j}$ describes the cosine of the angle between the transition dipole moments $\boldsymbol{\mu}_{e_i}$ and $\boldsymbol{\mu}_{e_j}$.

Fourier transforming S^k along the τ_1 and τ_3, along with remembering contour integration gives the non-linear response functions in the mixed frequency-time domain which allows us to calculate the 2DIR spectrum, yields

$$S^{k_R}_{v_4 v_3 v_2 v_1}(\omega_3, T_2, \omega_1) = 2i \sum_{e_4 e_3 e_2 e_1} M^{v_4 v_3 v_2 v_1}_{e_4 e_3 e_2 e_1} \times I^*_{e_1}(T_2) I_{e_2}(T_2) \mathfrak{T}_{e_4}(\omega_3) \mathfrak{T}^*_{e_1}(-\omega_1) \times \\ \Gamma_{e_4 e_1, e_3 e_2}(\omega_3 + \varepsilon_{e_1} + i\gamma_{e_1}) \mathcal{J}_{e_3 e_2}(\omega_3 + \varepsilon_{e_1} + i\gamma_{e_1})$$

(C1)

and

$$S^{k_{NR}}_{v_4 v_3 v_2 v_1}(\omega_3, T_2, \omega_1) = 2i \sum_{e_4 e_3 e_2 e_1} M^{v_4 v_3 v_2 v_1}_{e_4 e_3 e_2 e_1} \times I_{e_1}(T_2) I^*_{e_2}(T_2) \mathfrak{T}_{e_4}(\omega_3) \mathfrak{T}_{e_1}(\omega_1) \times \\ \Gamma_{e_4 e_2, e_3 e_1}(\omega_3 + \varepsilon_{e_2} + i\gamma_{e_2}) \mathcal{J}_{e_3 e_1}(\omega_3 + \varepsilon_{e_2} + i\gamma_{e_2}).$$

(C13)

The Fourier transformed Green functions are

$$\mathfrak{T}_{e'}(\omega) = \frac{i}{\omega - \varepsilon_{e'} + i\gamma_{e'}}$$

(C14)

and $\mathcal{J}_{e' e''}$ is the two-exciton Green function

$$\mathcal{J}_{e'e''}(\omega) = \frac{i}{\omega - \varepsilon_{e'} - \varepsilon_{e''} + i(\gamma_{e'} + \gamma_{e''})}. \tag{C15}$$

$\Gamma_{e_4 e_3, e_2 e_1}$ is the scattering of excitons written in an exciton basis. Calculating $\Gamma_{e_4 e_3, e_2 e_1}$, however, involves the interactions of excitations at local sites, thus we calculate $\Gamma_{e_4 e_3, e_2 e_1}$ by transforming from a site basis scattering matrix $\Gamma_{m,n}^{site}$,

$$\Gamma_{e_4 e_3, e_2 e_1}(\omega) = \sum_{m,n} \psi^*_{e_4 m} \psi^*_{e_3 m} \Gamma^{site}_{m,n} \psi_{e_2 n} \psi_{e_1 n}. \tag{C16}$$

The size of $\Gamma_{e_4 e_3, e_2 e_1}$ is greatly reduced when we only consider elements where excitons $e_4 e_3$ overlap and where excitons $e_2 e_1$ overlap. We define an exciton overlap factor,

$$\eta_{e,e'} = \sum_m |\psi_{e,m}| |\psi_{e',m}|, \tag{C17}$$

which relates the spatial overlap of each pair of excitons via the sites they occupy. We eliminate elements of $\Gamma_{e_4 e_3, e_2 e_1}$ by choosing a hard cutoff and only calculating $\Gamma_{e_4 e_3, e_2 e_1}$ where $\eta_{e_4 e_3}$ and $\eta_{e_2 e_1}$ are greater than the cutoff.

The site basis scattering matrix is calculated as

$$\Gamma^{site}_{m,n}(\omega) = -i \bar{\Delta}_m (\bar{D}^{-1})_{m,n} \tag{C18}$$

where $\bar{\Delta}_m$ is the anharmonic shift at site m, and $\bar{D}$ is

$$\bar{D}_{m,n} = \delta_{mn} + i \mathcal{G}_{m,n} \bar{\Delta}_n. \tag{C19}$$

The matrix $\mathcal{G}_{m,n}$ is a two-exciton Green function written in the site basis,

$$\mathcal{G}_{m,n}(\omega) = \sum_{e',e''} \psi_{e'm} \psi_{e''m} \mathcal{J}_{e'e''}(\omega) \psi^*_{e'n} \psi^*_{e''n}. \tag{C20}$$

In principle, $\mathcal{G}$ would be a tetradic matrix involving four sites. However, due to the local nature of the anharmonicity, meaning the site energy is only lowered on double excitations on the same site, we can reduce the size of $\mathcal{G}$ to an N×N matrix.

REFERENCES

[1] T. MIYAZAWA, J. Chem. Phys. **32**, 1647 (1960).

[2] S. Krimm and J. BANDEKAR, Adv. Protein Chem. **38**, 181 (1986).

[3] H. Torii and M. Tasumi, J. Raman Spectrosc. **29**, 81 (1998).

[4] A. Barth and C. Zscherp, Q. Rev. Biophys. **35**, 369 (2002).

[5] J.W. Brauner, C. Dugan, and R. Mendelsohn, J. Am. Chem. Soc. **122**, 677 (2000).

[6] J. Kubelka and T.A. Keiderling, J. Am. Chem. Soc. **123**, 12048 (2001).

[7] G. Zandomeneghi, M.R.H. Krebs, M.G. McCammon, and M. Fändrich, Protein Sci. **13**, 3314 (2009).

[8] S.A. Oladepo, K. Xiong, Z. Hong, S.A. Asher, J. Handen, and I.K. Lednev, Chem. Rev. **112**, 2604 (2012).

[9] K.M. Towle, C.T. Lohans, M. Miskolzie, J.Z. Acedo, M.J. van Belkum, and J.C. Vederas, Biochemistry **55**, 4798 (2016).

[10] E. Tayeb-Fligelman, O. Tabachnikov, A. Moshe, O. Goldshmidt-Tran, M.R. Sawaya, N. Coquelle, J.-P. Colletier, and M. Landau, Science (80-.). **355**, 831 (2017).

[11] E. Tayeb-Fligelman, N. Salinas, O. Tabachnikov, and M. Landau, Structure **28**, 301 (2020).

[12] S.A. Cracchiolo O, Edun D, Betti V, Goldberg J, ChemRxiv. Cambridge Cambridge Open Engag. (2021).

[13] H. Torii and M. Tasumi, J. Chem. Phys. **96**, 3379 (1992).

[14] S.H. Lee and S. Krimm, Chem. Phys. **230**, 277 (1998).

[15] Z. Ganim and A. Tokmakoff, Biophys. J. **91**, 2636 (2006).

[16] H. Torii and M. Tasumi, J. Chem. Phys. **97**, 92 (1992).

[17] H. Torii and M. Tasumi, J. Chem. Phys. **97**, 86 (1992).

[18] H.S. Chung and A. Tokmakoff, J. Phys. Chem. B **110**, 2888 (2006).

[19] D. Abramavicius and S. Mukamel, J. Chem. Phys. **122**, 134305 (2005).

[20] D. Abramavicius and S. Mukamel, Chem. Phys. **318**, 50 (2005).

[21] S. Mukamel, *Principles of Nonlinear Optical Spectroscopy* (Oxford University Press, New York, New York, 1998).

[22] W. Zhuang, D. Abramavicius, T. Hayashi, and S. Mukamel, J. Phys. Chem. B **110**, 3362 (2006).

[23] J.W.S. Hearle, J. Appl. Polym. Sci. **7**, 1175 (1963).

[24] J. Wang and R.M. Hochstrasser, Chem. Phys. **297**, 195 (2004).

[25] S. Mukherjee, P. Chowdhury, and F. Gai, J. Phys. Chem. B **111**, 4596 (2007).

[26] A.M. Dwivedi and S. Krimm, J. Phys. Chem. **88**, 620 (1984).

[27] J.H. Choi, S. Ham, and M. Cho, J. Chem. Phys. **117**, 6821 (2002).

[28] S. Woutersen and P. Hamm, J. Chem. Phys. **115**, 7737 (2001).

[29] M.R. Panman, C.N. van Dijk, H. Meuzelaar, and S. Woutersen, J. Chem. Phys. **142**, 041103 (2015).

[30] L. Minnes, D.J. Shaw, B.P. Cossins, P.M. Donaldson, G.M. Greetham, M. Towrie, A.W. Parker, M.J. Baker, A.J. Henry, R.J. Taylor, and N.T. Hunt, Anal. Chem. **89**, 10898 (2017).

[31] M. Khalil, N. Demirdöven, and A. Tokmakoff, J. Phys. Chem. A **107**, 5258 (2003).

[32] S. Woutersen and P. Hamm, J. Phys. Chem. B **104**, 11316 (2000).

[33] D.Y. Vorobyev, C.-H. Kuo, D.G. Kuroda, J.N. Scott, J.M. Vanderkooi, and R.M. Hochstrasser, J. Phys. Chem. B **114**, 2944 (2010).

[34] R.M. Hochstrasser, Chem. Phys. **266**, 273 (2001).

[35] P. Hamm and M. Zanni, *Concepts and Methods of 2D Infrared Spectroscopy* (Cambridge University Press, Cambridge, 2011).

[36] V. Cervetto, J. Helbing, J. Bredenbeck, and P. Hamm, J. Chem. Phys. **121**, 5935 (2004).

[37] A. Huerta-Viga and S. Woutersen, J. Phys. Chem. Lett. **4**, 3397 (2013).

[38] M.R. Panman, C.N. van Dijk, H. Meuzelaar, and S. Woutersen, J. Chem. Phys. **142**, 041103 (2015).

[39] O.M. Cracchiolo, D.N. Edun, V.M. Bretti, J.M. Goldberg, and A.L. Serrano, Submitt. Publ. (n.d.).

[40] S. Irgen-Gioro, K. Gururangan, R.G. Saer, R.E. Blankenship, and E. Harel, Chem. Sci. **10**, 10503 (2019).

[41] M.J. Nee, C.R. Baiz, J.M. Anna, R. McCanne, and K.J. Kubarych, J. Chem. Phys. **129**, 084503 (2008).

[42] M. Khalil, N. Demirdöven, A. Tokmakoff, N. Demirdöven, and A. Tokmakoff, J. Chem. Phys. **121**, 362 (2004).

[43] Y.-C. Cheng and G.R. Fleming, J. Phys. Chem. A **112**, 4254 (2008).

[44] T.R. Calhoun, N.S. Ginsberg, G.S. Schlau-Cohen, Y.-C. Cheng, M. Ballottari, R. Bassi, and G.R. Fleming, J. Phys. Chem. B **113**, 16291 (2009).

[45] E.A. Arsenault, Y. Yoneda, M. Iwai, K.K. Niyogi, and G.R. Fleming, Nat. Commun. **11**, 1460 (2020).

[46] E. Thyrhaug, K. Žídek, J. Dostál, D. Bína, and D. Zigmantas, J. Phys. Chem. Lett. **7**, 1653 (2016).

[47] E. Thyrhaug, R. Tempelaar, M.J.P. Alcocer, K. Žídek, D. Bína, J. Knoester, T.L.C. Jansen, and D. Zigmantas, Nat. Chem. **10**, 780 (2018).

[48] J. Cao, R.J. Cogdell, D.F. Coker, H.-G. Duan, J. Hauer, U. Kleinekathöfer, T.L.C. Jansen, T. Mančal, R.J.D. Miller, J.P. Ogilvie, V.I. Prokhorenko, T. Renger, H.-S. Tan, R. Tempelaar, M. Thorwart, E. Thyrhaug, S. Westenhoff, and D. Zigmantas, Sci. Adv. **6**, eaaz4888 (2020).

[49] J. Lim, D. Paleček, F. Caycedo-Soler, C.N. Lincoln, J. Prior, H. von Berlepsch, S.F. Huelga, M.B. Plenio, D. Zigmantas, and J. Hauer, Nat. Commun. **6**, 7755 (2015).

[50] D. Abramavicius, B. Palmieri, D. V. Voronine, F. Šanda, and S. Mukamel, Chem. Rev. **109**, 2350 (2009).

[51] C.M. Cheatum, A. Tokmakoff, and J. Knoester, J. Chem. Phys. **120**, 8201 (2004).